Lévy walk of quasiballistic phonons in nanowires

Jincui Li,[1] Linxi Weng,[1] Jie Xie,[1] Jay Amrit,[2] and Aymeric Ramiere[1,*]
[1]*College of Physics and Optoelectronic Engineering, Shenzhen University, Shenzhen 518060, China*
[2]*Laboratoire Interdisciplinaire des Sciences du Numérique, CNRS, Université Paris-Saclay, Rue du Belvédère, 91405 Orsay, France*

(Received 14 February 2022; accepted 31 May 2022; published 21 June 2022)

Phonon transport in square-cross-section nanowires is studied using spectral Monte Carlo simulations. Our results show the evolution of the different transport regimes described by Lévy statistics as a function of the surface roughness–to–thermal wavelength ratio σ/λ. More precisely, the relationship between the Lévy index γ describing the mean free path distribution $\Psi(\Lambda)$ and σ/λ is established for the classical diffusive regime, the superdiffusive regime, and the ballistic regime in the nanowire. Besides the conventional superdiffusive regime that is marked by $\Psi(\Lambda)$ with a single heavy-tailed peak, we reveal an unconventional superdiffusive subregime featuring $\Psi(\Lambda)$ with sawtooth oscillations when $\sigma/\lambda \sim 0.01$. Investigation of the direction of propagation of phonons shows a significant narrowing of the angular distribution around the long axis of the nanowire due to the diffuse scattering at rough boundaries when $\sigma/\lambda > 0.1$. These results shed light on the transport mechanisms of quasiballistic phonons and will help in nanowire design for specific applications.

DOI: 10.1103/PhysRevE.105.064123

I. INTRODUCTION

In the quasiparticle picture of phonons (heat carriers), thermal conductivity in dielectric materials is controlled by phonon diffusion. As the size of the material decreases to attain nanostructure dimensions, the surface-to-volume ratio increases and the boundary scattering plays a major role in phonon diffusions [1]. The phonon excursion lengths between diffusions, or mean free paths (MFPs) Λ, are crucial in determining the material's thermal properties [2]. In reality, phonon MFPs follow Lévy statistics [3] and are characterized by the probability density function (PDF) $\Psi(\Lambda)$, which for large Λ decays as

$$\Psi(\Lambda) \sim \Lambda^{-\gamma-1}. \tag{1}$$

The Lévy index γ tunes the different diffusion regimes. Classical heat diffusion, described by Fourier's law, is characterized by short MFPs and narrow PDF due to the primacy of diffuse interactions and is observed for $\gamma \geqslant 2$ corresponding to a traditional random-walk behavior of the phonon gas. As diffuse interactions decrease, longer MFPs are allowed, therefore broadening the PDF. When $1 \leqslant \gamma < 2$ the phonon transport is called superdiffusive as phonons can reach farther distances than in the classical diffusion. The dramatic change occurs in the extreme ballistic regime where the phonon MFPs can exceed the sample size for $0 \leqslant \gamma < 1$. For this case, the local thermodynamic equilibrium is now compromised [4,5]. Consequently, Fourier's law is no longer valid and the thermal conductivity ceases to be an intrinsic property of the material since it now acquires a size dependence [6,7].

When the phonon MFP exceeds the characteristic dimension in nanostructures, phonons can travel ballistically from boundary to boundary and therefore experience diffusions mainly because of the boundary surface roughness. These phonons are qualified as quasiballistic. Such phonons have been recently observed experimentally in semiconductor nanowires [8,9]. These experiments demonstrated that the phonon MFP could be extremely long, up to tens of micrometers, even in nanowires with nanometer-size diameters [10]. This quasiballistic behavior is usually detected by a rise in thermal conductivity with the nanowire's length [11,12]. In nanowires fabricated by the bottom-up approach with very smooth walls, the ballistic heat transport persists at scale lengths of 8 μm in SiGe nanowires [13] and very recently beyond 15 μm in GaP nanowires [14]. The top-down approach offers more flexibility to conceive complex designs like phononic nanostructures. However, this technique generates nanowires with rougher surfaces and the ballistic heat transport is observed at lower temperatures or in shorter nanowires [15,16]. Although it is admitted that an increased surface roughness reduces the thermal conduction, little is known about how the roughness modifies the propagation of the quasiballistic phonons inside rough nanowires and the associated transport mechanisms.

This paper focuses on the influence of surface roughness on the phonon transport mechanisms in nanowires with a square cross section. As discussed above, the Lévy index γ serves as a useful parameter for describing anomalous diffusion regimes. The control of γ is essential to optimize phonon transport and heat dissipation at the nanoscale [17–19]. In this work, using Monte Carlo simulations, we demonstrate that γ can in fact be adjusted by two parameters, namely, the surface roughness and the thermal phonon wavelength. More precisely, we show that the various diffusion regimes can be targeted by setting the surface roughness–to–thermal phonon wavelength ratio. The surface roughness is an extrinsic parameter that can be controlled depending on the fabrication

*ramiere@szu.edu.cn

techniques. The thermal phonon wavelength is an intrinsic parameter determined by the temperature and the sound velocity in the material.

The rest of the paper is organized as follows. Section II describes our numerical approach of the three-dimensional (3D) ray-tracing Monte Carlo technique and the different key parameters related to scattering probabilities at boundaries. In Sec. III we present a qualitative analysis of the scattering rates of phonons as a function of their wavelengths for different surface roughnesses. The angular distribution of transmitted phonons is also discussed. Section IV presents our main results on the change in the accumulated thermal conductivity and the MFP distributions for different roughnesses and thermal wavelengths. From these results, the different Lévy regimes are identified as a function of the roughness-to-wavelength ratio. This is our key result, which gives a qualitative description of how surface roughness modifies phonon diffusion within a nanowire, resulting in the different transport regimes.

II. SPECTRAL MONTE CARLO SIMULATIONS

Ray-tracing simulations were carried out using the Monte Carlo technique to follow the 3D trajectories of phonons in rough nanowires with square cross sections. Nanowires with square cross sections are usually fabricated by structuring a thin film of material using nanolithography techniques. This fabrication process results in significant differences between the roughness at the side surfaces and the roughness at the top and bottom surfaces [15,20]. We separate the surface roughness of the top and bottom walls, denoted by σ_t, and the surface roughness of the sidewalls, denoted by σ_s, to account for this effect, as depicted in Fig. 1(a). The top and bottom surfaces are usually unaffected by the nanofabrication process and remain very smooth, with a roughness below 1 nm. In our case, we set $\sigma_t = 0.5$ nm, following experimental measurements on silicon nanostructures [21]. For the side surfaces, σ_s can reach several nanometers and depends on the nanofabrication process [22–26]. Here we carry out simulations for a range of possible σ_s from 1 to 4 nm.

Our simulations target dielectric materials where phonons carry heat. We examine the quasiballistic phonon transport mediated only by boundary scattering; internal scattering such as impurity scattering, phonon-phonon processes, and interactions with surface excitations are considered negligible. The nanowire links a hot reservoir to a cold reservoir. The phonons are emitted by the hot reservoir with initial angles of propagation (θ, ϕ) that are randomly assigned with uniform probability. In the next step, the phonon moves to the nearest geometrical boundary that intersects with its trajectory. There the phonon will randomly scatter either specularly or diffusively.

According to Ziman's theory, we suppose that phonons are described by plane-wave packets that are large enough to be considered as nearly monochromatic with a wavelength λ, but small enough to experience small perturbations by the surface roughness σ [27]. This surface roughness is characterized by a random distribution of heights with a Gaussian probability and satisfy the Kirchhoff approximation with a correlation length exceeding the wavelength [28]. The

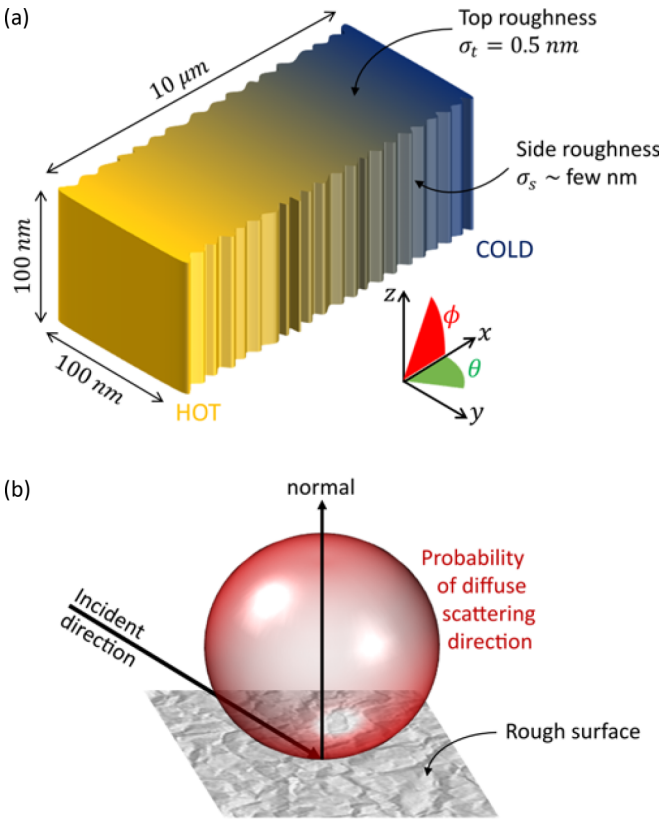

FIG. 1. (a) Schematics of square-cross-section nanowire illustrating the top and bottom roughness and the side roughness. (b) Representation of Lambert's cosine law, which gives the probability of the scattered angle upon a diffuse scattering event on a rough surface.

specularity parameter gives a phonon the probability of undergoing a specular scattering event at the boundary. Here we use the angle-dependent specularity parameter given by

$$P_S = \exp\left(-16\pi^2 \frac{\sigma^2}{\lambda^2} \cos^2 A_i\right), \tag{2}$$

where σ is the surface roughness, λ is the wavelength, and A_i is the incident angle with the normal of the average surface of the nanowire at the scattering site [29]. Equation (2) suggests that the incident angle plays an essential role in the quasiballistic phonon transport as a larger A_i yields a higher P_S. The diffuse or specular nature of the scattering is determined by a random number picked between 0 and 1. If this random number is smaller than P_S, the scattering is specular and the phonon is mirror reflected; otherwise, the scattering is diffuse and the phonon changes direction randomly.

The diffuse scattering process randomizes the direction of propagation of the phonons in the nanowire. The diffuse angle is picked following Lambert's cosine law, which is classically used to qualify photon reflection on rough surfaces [30]. This law allows diffused phonon to go in any direction, but it gives a higher probability to the directions around the normal to the surface, as illustrated in Fig. 1(b). This randomization of the angles is responsible for the backscattering of phonons and creates a temperature gradient in the nanowire [5]. Overall, the phonons can travel back and forth between boundaries many

times before reaching one of the reservoirs. If the phonon arrives at the cold reservoir, it is counted as transmitted, and if it returns to the hot reservoir, it is counted as backscattered.

The spectral properties of the phonons are studied by sweeping the wavelength from 0.5 to 5000 nm. The shortest wavelength corresponds to the typical dimension of the unit cell of most crystalline materials. The longest wavelength is chosen so phonon transmission reaches unity, as we will show later while minimizing the phonon confinement effects [31]. Though other scattering phenomena may occur besides the boundary scattering for the extreme values of the simulated wavelengths, the same set of rules is applied for the whole spectrum to allow a direct comparison of the results.

Notice that in the boundary scattering regime, the physics of phonon transport is ruled by Eq. (2) and Lambert's cosine law, which do not need information about the temperature and material properties as we work with spectral quantities. Therefore, the results of our simulations apply to any material at all temperatures. However, the fraction of phonons in the boundary scattering regimes depends on the material and the temperature. For example, for a silicon nanowire with a characteristic length of 100 nm like in our case, the boundary scattering regime dominates for a wide temperature range from 1 to 110 K [32]. This temperature range shifts to higher temperatures as the characteristic dimension is reduced.

The dimensions of the nanowire are set to a square cross section of $100 \times 100\ \text{nm}^2$ and a length $L = 10\ \mu\text{m}$. The sidewall's roughness σ_s is varied from 1 to 4 nm. This geometry and the roughnesses are chosen to provide sufficient diffusive scattering events to ensure that the collective diffusive regime is reached, especially for short wavelengths. Statistical data are collected for the transmitted phonons that participate in the heat transfer from the hot to the cold reservoir. Here $N_{\text{tot}} = 10^7$ phonons per wavelength are simulated to accumulate sufficient statistics and obtain smooth data across all the wavelengths.

During the simulations, statistical quantities of the propagation properties of phonons in the nanowire are registered, such as the specular scattering rate, the number of scattering events, the phonon transmission, the output angles, and the distribution of MFPs. The specular scattering rate $S_{\text{tot}}(\lambda)$ is defined as the ratio of specular scattering events over the total number of scattering events in the nanowire. For more details, we also determine the specular scattering rate individually at the rough side wall boundaries $S_s(\lambda)$ and at the smooth top and bottom wall boundaries $S_t(\lambda)$. The number of scattering events at each boundary is also recorded such that $N_{\text{tot}} = N_s + N_t$, where N_s, N_t, and N_{tot} are the number of scattering events at the sidewalls, at the top and bottom walls, and in total. The phonon transmission $\tau(\lambda)$ is the number of phonons arriving at the cold reservoir divided by the number of phonons simulated per wavelength. Finally, we gather statistics on the angles at which the phonons reach the cold reservoir to observe the transformation from the initial uniform angular distribution at the hot reservoir.

The MFP $\Lambda_{\lambda,k}$ is the length traveled by a phonon of wavelength λ between two diffuse scattering events. The subscript k is used to sort the MFPs by intervals of 2 nm length from 0 to 30 μm such that $2k < \Lambda_{\lambda,k} < 2(k+1)$ nm. The MFP distribution is obtained by taking the number $N(\Lambda(\lambda, k))$ of MFPs in each interval. This definition of the MFP distribution is in fact the PDF $\Psi(\Lambda)$ that can be analyzed using Eq. (1) to identify the transport regimes. The MFP distribution is then used to determine the accumulated thermal conductivity (ATC)

$$\alpha(\Lambda_{\lambda,i}) = \frac{\sum_{k=0}^{m} N(\Lambda_{\lambda,k})}{\sum_{k=0}^{\infty} N(\Lambda_{\lambda,k})}, \tag{3}$$

which describes the fraction of the total thermal conductivity due to phonons with MFPs less than $\Lambda(\lambda, m)$ [33]. The ATC can be reconstructed from experimental measurements and be compared with simulations [34].

III. PHONON DYNAMICS AS QUASIPARTICLES WITHIN A NANOWIRE

A. Scattering rates at boundaries and energy transmission

Figures 2(a), 2(b), and 2(c) show the spectral specular rates S_t, S_s, and S_{tot}, respectively. The specular rates start close to 0 at the shortest wavelengths as almost all phonons undergo diffusive scattering. As the wavelengths increase, there is a transition to greater specular scattering events until all scattering events become specular ($S = 1$) at long wavelengths. The curves at the top and bottom walls in Fig. 2(a) are identical because all the nanowires have the same roughness at the top and bottom walls, $\sigma_t = 0.5$ nm. We compare the simulation with the theoretical specularity parameter given in Eq. (2) using a roughness of 0.5 nm and different incident angles A_i from 0° to 80° [see gray lines in Fig. 2(a)]. The specularity parameter with $A_i = 40°$ gives the best fit for $\lambda > 10$ nm, but this fit falls below the simulations for shorter wavelengths. The incident angle in Eq. (2) must then be increased progressively as the wavelength decreases to match the simulations. Physically, this means that the average angles of the phonons become centered along the x axis of the nanowire as the wavelength shortens.

An increase in incident angles similar to that in Fig. 2(a) is also observed in Fig. 2(b) for the sidewall specular rate. For each sidewall roughness σ_s, the dashed line represents Eq. (2) with the best angle A_i that fits the specular rate at long wavelengths. The obtained angles show that a higher roughness yields a larger angle closer to the x axis which is the long axis of the nanowire. Therefore, the roughness changes the overall direction of propagation of the phonon flow in the nanowire.

The centering of the direction of propagation around the x axis stems from diffuse scattering. With a higher roughness, a phonon has a higher probability of being diffusively scattered and each diffuse scattering randomizes the direction of propagation of the phonon. The same phenomenon occurs when the wavelength decreases because the specularity parameter decreases as the wavelength shortens. Therefore, the increase of the angle A_i seems correlated to the diffusivity that allows phonons with a direction near the x axis to propagate more easily through the nanowire. Further studies of the angles of the phonons that exit the nanowire will confirm this view in the next section.

Figure 2(c) shows the total specular rates in the nanowire for all four walls. In the case of isotropic propagation of

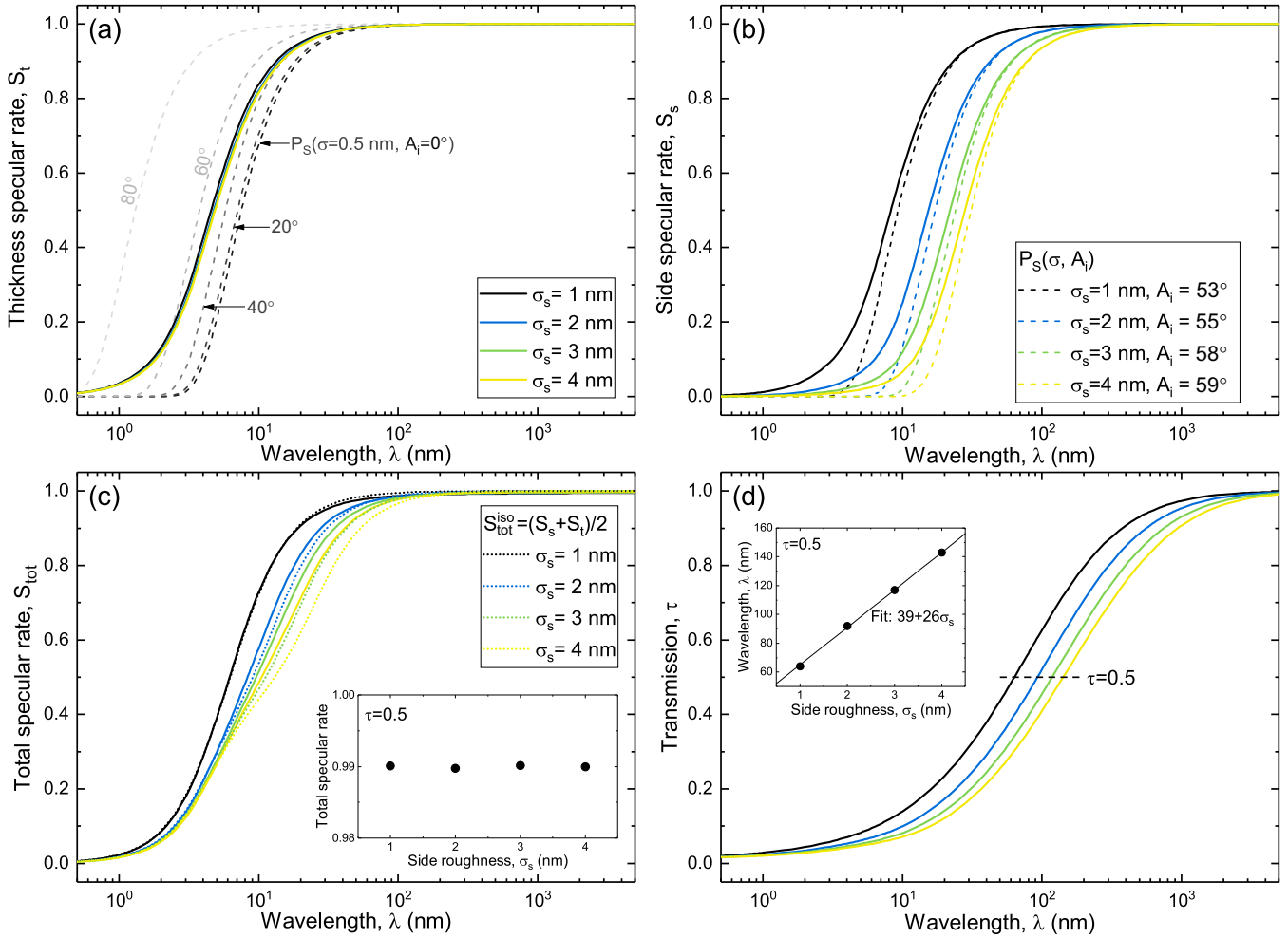

FIG. 2. (a) Specular scattering rates at the smooth top and bottom walls. Gray lines are obtained with Eq. (2) using a roughness of 0.5 nm and different incident angles as indicated. (b) Specular scattering rate at the rough sidewall boundaries. The dashed lines were also obtained with Eq. 2. (c) Total specular rate in the nanowire. The dotted lines represent the isotropic rate $S_{\rm tot}^{\rm iso} = (S_s + S_t)/2$. The inset shows $S_{\rm tot}$ at $\tau = 0.5$. (d) Transmission rate of phonons to the cold reservoir. The inset shows the linear relation between the wavelength at $\tau = 0.5$ and the sidewall roughness.

phonons in the square-cross-section nanowire, one expects a balanced scattering rate between the top and bottom walls and the sidewalls such that $S_{\rm tot}^{\rm iso} = (S_t + S_s)/2$, as depicted by the dotted lines in Fig. 2(c). However, the simulated total specular rate $S_{\rm tot}$ significantly deviates from this average, especially in the intermediate-wavelength range, demonstrating an imbalance in the scattering events between the sidewalls and the top and bottom walls. The observed total specular rate is higher than the isotropic average, indicating that more scattering events occur at the smooth top and bottom walls than at the rougher sidewalls. This difference increases with the sidewall roughness since the roughness drives the imbalance in the boundary scattering processes between these two types of walls. Therefore, the phonons' propagation direction becomes anisotropic as they progress in the nanowire.

In Fig. 2(d), the transmission coefficient versus the thermal wavelength shows a trend similar to that of the specular rates in Figs. 2(a)–2(c). However, the transition from $\tau \approx 0$ to $\tau \approx 1$ is much smoother such that the transmission coefficient is globally lower than the total specular rate. This shows that the specularity rate, and therefore Eq. (2), cannot explain the transmission coefficient alone. One aspect that is not considered in the specular rate [and Eq. (2)] is the direction of the propagation angle: forward (towards the cold reservoir) or backward (towards the hot reservoir). It is obvious that a phonon must have a forward direction to be transmitted. For example, even if the specular rate is close to 1 and the phonon moves forward bouncing specularly between boundaries, one single diffuse scattering event is enough to reverse the sense of direction. The phonon then goes backward with an identical specular rate.

The transmission increase with the wavelength indicates that specularity favors phonons to move forward, toward the cold side, against the backward flow initiated by diffusivity. The equilibrium between these forward and backward flows occurs at $\tau = 0.5$. The inset in Fig. 2(d) shows that the wavelength at half transmission $\lambda(\tau = 0.5)$ increases linearly with the side roughness, in agreement with previous simulations in 2D nanowires [32]. The linearity is the consequence of the specularity parameter (2), which is determined by the roughness-to-wavelength ratio σ/λ. The inset in Fig. 2(c) shows the total specular rate $S_{\rm tot}$ for the wavelength

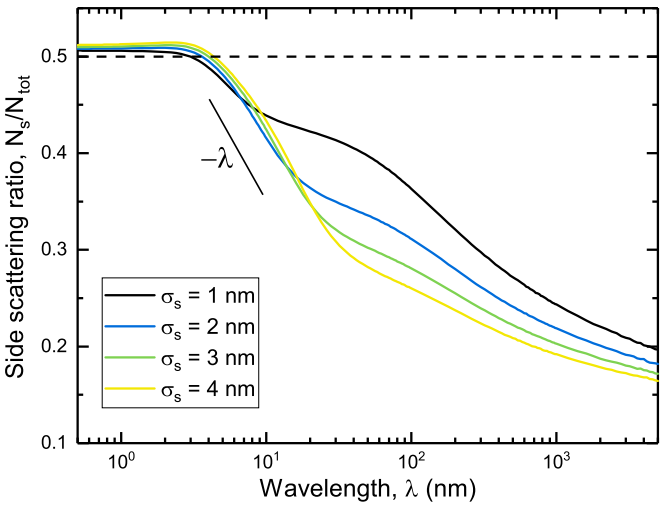

FIG. 3. Spectral evolution of the fraction of scattering events at the sidewall boundaries N_s/N_{tot}.

at half transmission $\lambda(\tau = 0.5)$. Most interestingly, we find a constant rate $S_{\text{tot}} = 0.99$, independent of the roughness. This means that only 1% of diffuse scattering events in the nanowire is enough to backscatter half the phonons to the hot reservoir. This clearly illustrates that the backward flow created by diffuse scattering is greater than the forward flow due to specular scattering.

To understand the imbalanced scattering process between the top and bottom walls and the sidewalls observed in Fig. 2(c), we consider the specular evolution of the ratio N_s/N_{tot}, where N_{tot} and N_s are the total number of scattering events in the nanowire and the number of scattering events at the sidewalls, respectively. In Fig. 3, N_s/N_{tot} remains at a constant value of 0.51 for $\lambda \lesssim 4$ nm, indicating that phonons scatter back and forth almost equally between the sidewalls and the top and bottom wall boundaries. From $\lambda \sim 4$ nm, the N_s/N_{tot} ratio drops abruptly, following the same linear trend with the wavelength for all the roughnesses. Then N_s/N_{tot} breaks to a milder decrease with the breakpoint occurring at a shorter wavelength for a lower roughness. The decrease of N_s/N_{tot} below 0.5 shows that the imbalance observed previously in the total specular scattering in Fig. 2(c) stems from phonons traveling more through the out-of-plane (x, z) rather than the in-plane (x, y). In addition, N_s/N_{tot} provides the ratio that must be used to reconstruct the total specular rate in Fig. 2(c) from Figs. 2(a) and 2(b).

B. Angular distribution of transmitted phonons

The specular rates in Figs. 2(a) and 2(b) suggest that the angular distribution of the phonons changes with their wavelength. To observe this phenomenon, we plot in Fig. 4 the angular distributions θ_{out} and ϕ_{out} of the phonons at the cold end of the nanowire for four wavelengths: $\lambda = 1$, 10, 100, and 1000 nm. Globally, for both θ_{out} and ϕ_{out}, the smaller the wavelength, the narrower the distribution around 0°. Following our conventions, $\theta_{\text{out}} = 0°$ is along the x direction, parallel to the sidewall boundaries, representing an angle of 90° in the specularity parameter (2). Therefore, shorter wavelengths yield phonons that arrive on the boundary with a higher angle of incidence, thus explaining the results of the specularity rates in Fig. 2.

In Figs. 4(a) and 4(b), for $\lambda = 1$ nm, the distributions have less than a few degrees of variation around 0°, indicating that phonons propagate almost exclusively with directions parallel to the x axis. At this wavelength, almost all scattering events are diffuse and Lambert's cosine law, which favors scattering angles perpendicular to the x axis, should generate θ_{out} and ϕ_{out} close to 90°. However, diffusively scattered phonons scatter more often on the boundaries because they have a higher probability of attaining a perpendicular direction. Though the probability to obtain an angle close to 0° is very small, once such an angle is drawn, the phonons have a very high probability to retain it because the specularity parameter is higher and also because the phonon experiences fewer scattering events, which reduces the opportunities to modify this angle. Finally, since our nanowire has a very high length-to-width ratio, the very large number of diffuse scattering events transform the initial isotropic angular distribution at the hot reservoir into a very narrow distribution where only phonons with very small angles are able to reach the cold reservoir.

At the opposite end of the wavelength range, in Figs. 4(g) and 4(h), the near-isotropic distribution at $\lambda = 1000$ nm reflects the initial isotropic random distribution of the angles that is maintained up to the cold reservoir because of the very high specularity. Figures 4(c)–4(f) shows that for intermediate wavelengths the angular distribution broadens as the wavelength increases. Figures 4(c) and 4(e) display a dip for all θ around 0° for the intermediate wavelengths. This dip is explained by the combination of specular and diffuse scattering that allows better transmission of intermediate angles than angles around 0° that have a very low probability of appearing during a diffusion. This phenomenon seems to disappear at short wavelengths when angles are randomized and at long wavelengths where diffuse scattering vanishes.

Globally, the roughness-to-wavelength ratio σ/λ determines the angular behavior as it plays a major role in Eq. (2). It can be interpreted that the diffuse scattering generates a selection process where only phonons with angles around the x axis can propagate through the nanowire [35]. By randomizing the angle at each diffuse scattering, the roughness allows the phonon to acquire a direction of propagation that avoids the boundaries. This direction is then preserved for a long distance and possibly beyond the nanowire, due to the negligible internal scattering in the quasiballistic regime. Therefore, the narrow exit angle distribution when $\sigma/\lambda > 0.1$ indicates that rough nanowires can be used to emit quasiballistic phonons with the direction of propagation along their long axis.

IV. OBSERVING LÉVY-WALK REGIMES

A. Mean free path and accumulated thermal conductivity distributions

We investigate the transport mechanisms which come into play in the nanowire by determining the ATC distribution $\alpha(\Lambda)$ and the PDF $\Psi(\Lambda)$. Figures 5(a)–5(h) show the evolution of the distributions $\Psi(\Lambda)$ and $\alpha(\Lambda)$ for four phonon

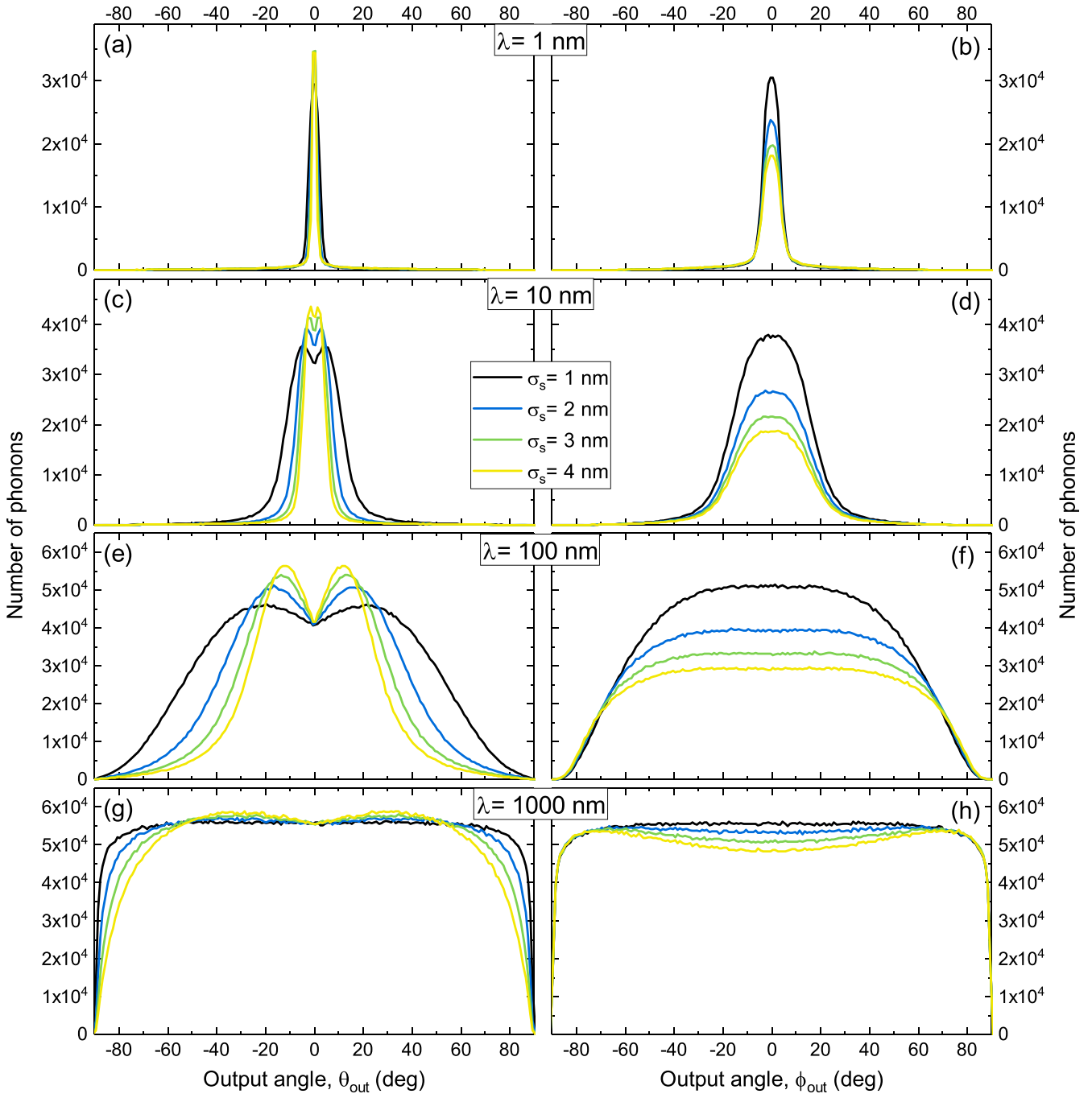

FIG. 4. Distribution of in-plane θ_{out} and out-of-plane ϕ_{out} exit angles at the cold end of the nanowire for different wavelengths: (a) and (b) $\lambda = 1$ nm, (c) and (d) $\lambda = 10$ nm, (e) and (f) $\lambda = 100$ nm, and (g) and (h) $\lambda = 1000$ nm.

wavelengths, namely, $\lambda = 1$, 10, 100, and 1000 nm. Also, in each of the figures, four different sidewall roughnesses are considered, namely, $\sigma_s = 1$, 2, 3, and 4 nm. The 10×10^6 simulated phonons provide a high resolution $\Psi(\Lambda)$ where fine structures become apparent such as peaks corresponding to preferential selection of specific mean free paths, which play a predominant role in phonon transport.

For phonons with thermal wavelengths $\lambda \leqslant 1$ nm [see Figs. 5(a) and 5(b)] the effect of the surface roughness is completely washed out and the curves overlap each other perfectly. For this phonon wavelength, the $\Psi(\Lambda)$ distribution shows a gradual decreasing contribution from all increasing Λ which lie within the range 1 nm $< \Lambda <$ 100 nm. However, at $\Lambda \approx 100$ nm, there is an abrupt increase in $\Psi(\Lambda)$, indicating that most phonons have a mean free path of $\sim$100 nm and that their displacements are limited by the lateral dimensions of the sample, as expected in the case where diffuse scattering prevails. Hereafter, the sharp decrease in $\Psi(\Lambda)$ with Λ testifies that a negligible amount of phonons have $\Lambda > 100$ nm. The $\alpha(\Lambda)$ distribution does indeed reach almost unity at $\Lambda = 100$ nm and nicely confirms that the thermal conductivity arises essentially from phonons having $\Lambda \approx 100$ nm. We also note that our accumulated thermal conductivity results are in good agreement with density functional theory (DFT) calculations

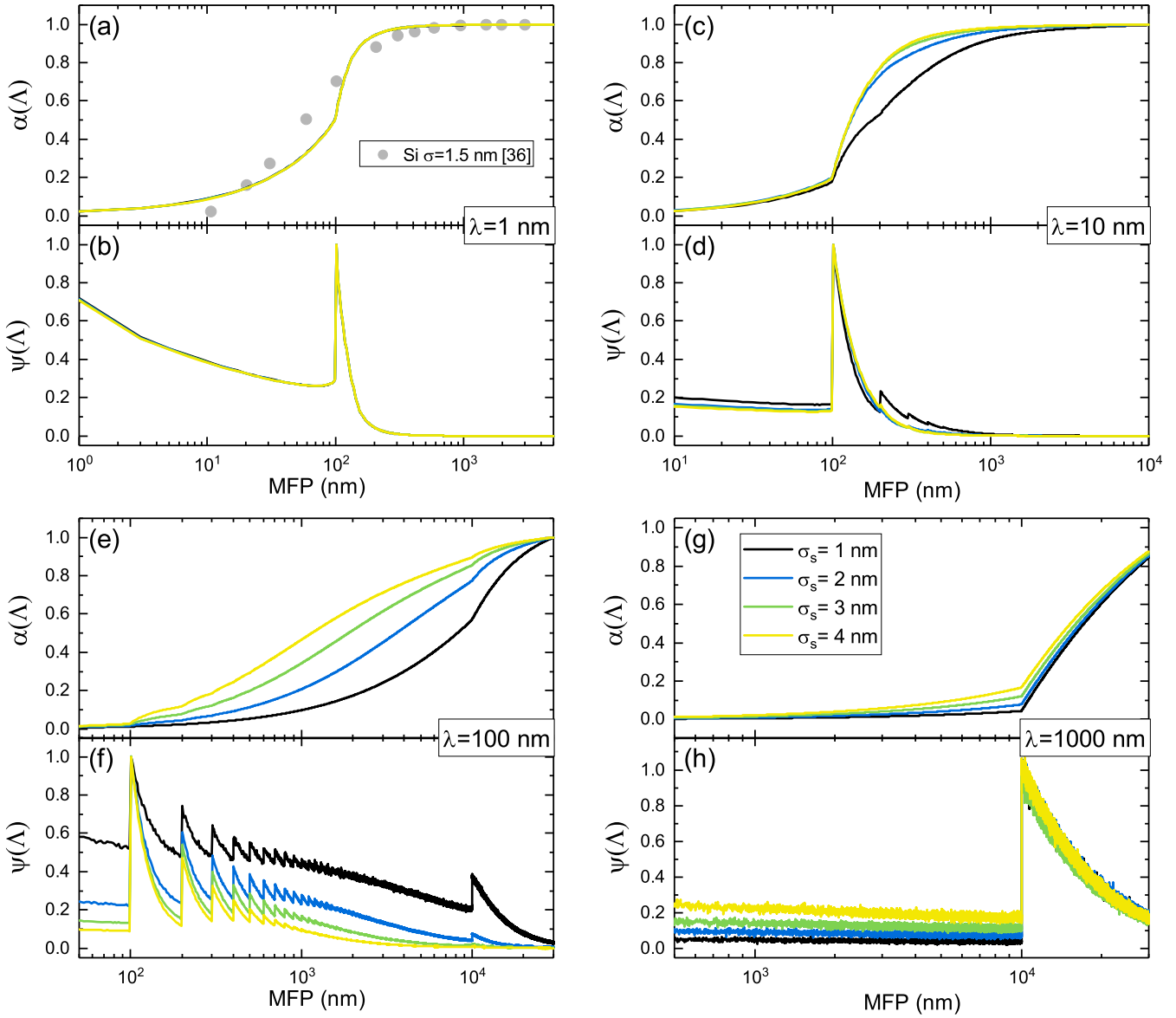

FIG. 5. ATC $\alpha(\Lambda)$ and PDF $\Psi(\Lambda)$ in nanowires with roughnesses $\sigma = 1$, 2, 3, and 4 nm at selected wavelengths. (a) and (b) $\lambda = 1$ nm. The ATCs are identical for each roughness and form one sharp peak in the PDF. Our ATC is in good agreement with DFT calculations on Si nanowire with roughness $\sigma = 1$ nm from Ref. [36]. (c) and (d) $\lambda = 10$ nm. The ATCs at different roughnesses separate for intermediate MFPs. In the PDF, mainly one peak appears with a heavy tail. (e) and (f) $\lambda = 100$ nm. The ATCs at different roughnesses separate further and sawtooth oscillations appear in the PDF. (g) and (h) $\lambda = 1000$ nm. The ATCs collapse again. One single broad peak in the PDF appears when the MFP reaches the length of the nanowire.

[see closed circles in Fig. 5(a)] at room temperature carried out on silicon nanowires of 100 nm diameter, where the surface roughness of 1.5 nm plays a dominant role [36].

In Figs. 5(c) and 5(d), for phonons with $\lambda = 10$ nm, the effects of surface roughness become visible. The $\Psi(\Lambda)$ distribution still shows a strong peak at 100 nm, decreasing slowly to form a heavy tail. This heavy tail is described in the literature as the signature of a superdiffusive phonon transport regime due to the Lévy walk [37,38]. More details about the tail will be discussed in the next section. We also note that the heavy tail drop is sensitive to surface roughness. Indeed, for the smallest roughness $\sigma_s = 1$ nm, tiny peaks appear in the heavy tail of the PDF, indicating that the increase of specular scattering not only increases the size of the tail but also starts transforming the phonon transport properties with the advent of other mechanisms that will become clearly visible at $\lambda = 100$ nm. The contributions from phonons with $\Lambda < 100$ nm are highly diminished compared to the case of phonons having $\lambda = 1$ nm, shown in Fig. 5(a). The $\alpha(\Lambda)$ distribution for $\sigma_s = 1$ nm differs from the other roughnesses due to contributions from Λ laying within the end of the heavy tail.

In Fig. 5(f), for $\lambda = 100$ nm, the $\Psi(\Lambda)$ distribution clearly displays a damped sawtooth oscillation behavior with a period $\Lambda = 100$ nm. This feature is characteristic of the presence of quasiballistic phonons which undergo several successive specular scattering events. According to Lambert's cosine law, angles normal to the surface are more probable, which

cause phonons to move from boundary to boundary by jumps with lengths close to the width of the nanowire $W_n = 100$ nm. Therefore, MFPs with lengths which are multiples of W_n are much more likely to occur, explaining the period of the oscillations every $\Lambda = 100$ nm. When the phonons arrive on a boundary, a fraction P_S [see Eq. (2)] of them continue their MFP while the others are diffusively scattered. Then the fraction P_S of specularly scattered phonons move to the next boundary where again a fraction P_S can pursue their MFP, etc. Therefore, fewer phonons have the possibility to increase their MFP after each scattering event, thus explaining the dampening of the oscillations. A generalization of the oscillation behavior is given in the Appendix. The total specular rate at $\lambda = 100$ nm in Fig. 2(c) indicates that a very high level of 95%–99% of scattering events (depending on the roughness) must be specular to obtain the sawtooth oscillations.

In Fig. 5(e), the impact of the oscillations is invisible in the $\alpha(\Lambda)$ distribution. This absence of characteristic oscillations in the $\alpha(\Lambda)$ distribution may explain why this phenomenon has been unnoticed. A possible way to observe these oscillations could be to measure precisely the thermal conductivity at very low temperatures and then use the MFP reconstruction method such that the derivative of the $\alpha(\Lambda)$, which gives the PDF $\Psi(\Lambda)$, has sufficient resolution to detect the oscillations.

In Fig. 5(f), peaks also appear in the $\Psi(\Lambda)$ distribution at $\Lambda = 10\,000$ nm for only the smaller roughnesses, namely, $\sigma_s = 1$ and 2 nm. The fact that Λ corresponds to the nanowire length is characteristic of the ballistic regime where phonons travel through the nanowire without experiencing any diffuse scattering.

In Figs. 5(g) and 5(h), for phonons with $\lambda = 1000$ nm, only a single peak at $\Lambda = 10\,000$ nm is observed, indicating that the ballistic regime entirely dominates the phonon transport in the nanowire. We also notice that the curves for the different roughnesses are superimposed, implying that the roughness no longer plays a role in the ballistic phonon transport.

B. Qualitative analysis of quasiballistic phonon transport mechanisms

In this section, we analyze the phonon transport mechanisms using the framework of the Lévy-walk models [3]. We show that a specific transport regime can be targeted in a controlled manner. Quasiballistic phonons can be viewed as noninteracting Lévy walkers and their behavior can be described statistically by the Lévy-walk model.

In this model, particle phonons alternate between ballistic flights during which they travel a long distance and rest phases during which they stay localized [39]. In our case, the rest phase corresponds to the phonon undergoing many diffuse scattering at the boundary, resulting in the phonon moving randomly forward and backward without going significantly in either direction. The PDF $\Psi(\Lambda)$ of the MFP (jump lengths) is characterized by decaying functions with power-law tails $\Psi(\Lambda) \sim \Lambda^{-\gamma-1}$ [see Eq. (1)]. As described in the Introduction, the Lévy index γ plays a decisive role in describing the regime that comes into play [40].

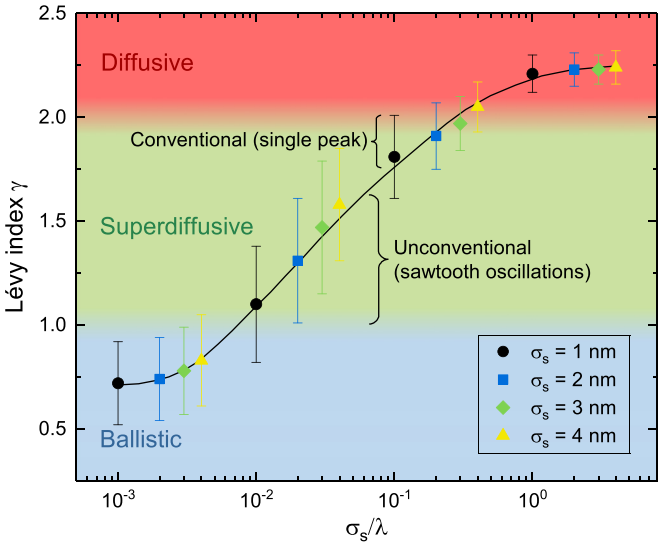

FIG. 6. Lévy index γ obtained by fitting the first peak in the MFP distribution: $\gamma > 2$, diffusive regime; $1 < \gamma < 2$, superdiffusive regime; and $\gamma < 1$, ballistic regime. Two subregimes are distinguished within the superdiffusive regime: the conventional superdiffusive regime characterized by a single heavy-tailed peak and the unconventional superdiffusive regime characterized by sawtooth oscillations. The black line is a guide for the eye.

We now establish the relationship between γ and the two variable parameters in the simulation, namely, the surface roughness σ_s and the thermal phonon wavelength λ. In Fig. 5, each PDF $\Psi(\Lambda)$ is established for four surfaces roughnesses σ_s at a given wavelength. The γ is obtained by fitting each of the four heavy tails of the first peak in the $\Psi(\Lambda)$ distribution with a power law. Figure 6 shows a clear transition from the fully ballistic regime where $\gamma \approx 0.7$ and $\sigma_s/\lambda < 0.01$ to the fully diffusive regime where $\gamma \approx 2.2$ and $\sigma_s/\lambda > 1$. In the intermediate region, the superdiffusive regime is clearly demonstrated. The error bars in the figure represent the uncertainty in the power-law fit.

According to the Lévy indices found in Fig. 6, it is clear that the sawtooth oscillations behavior observed in Fig. 5(f) belongs to the superdiffusive regime. Therefore, two subregimes should be distinguished within the superdiffusive regime: (i) the conventional superdiffusive regime located in the upper region with $0.01 < \sigma_s/\lambda < 0.1$ and $1.8 < \gamma < 2$ that is close to the diffusive regime and is characterized by a single heavy tail in the $\Psi(\Lambda)$ distribution and (ii) the unconventional superdiffusivce regime located in the lower region with $0.01 < \sigma_s/\lambda < 0.1$ and $1.0 < \gamma < 1.8$ that is characterized by sawtooth oscillations in the $\Psi(\Lambda)$ distributions.

For the oscillating $\Psi(\Lambda)$ distributions in Fig. 5(f), besides the first peak, the second and third peaks were also fitted with Eq. (1) to observe the evolution of the power exponent γ. Figure 7 shows that γ decreases with the peak number, indicating that the transport regime becomes more and more ballistic for successive sawtooth oscillations. Furthermore, γ decreases faster for larger σ_s/λ values. This decrease can be understood by narrowing the angle distribution around the x axis when phonons propagate through the rough nanowire,

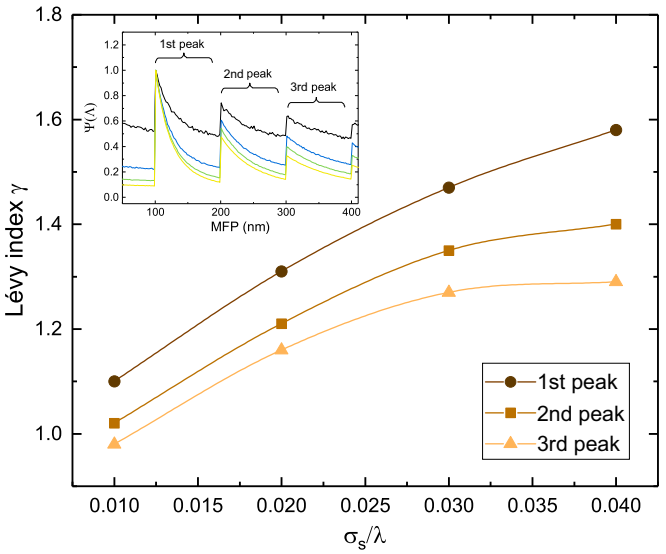

FIG. 7. Lévy index γ obtained for the first peak, second peak, and third peak of the MFP distribution at $\lambda = 100$ nm. The inset is a close-up of Fig. 5(f) around the first three peaks.

as we noticed previously. According to Eq. (2), when the direction of propagation is closer to the x axis, the angle A_i is larger, which increases the specularity probability and makes the transport closer to the ballistic regime.

V. CONCLUSION

Quasiballistic transport of particlelike phonons can be described by the Lévy-walk model and each transport regime that is operational is determined by the Lévy index. Using spectral Monte Carlo simulations in square-cross-section nanowires with different roughnesses, we have demonstrated that the roughness-to-wavelength ratio σ_s/λ controls the Lévy index. Consequently, the quasiballistic phonon transport can be tailored by targeting a specific σ_s/λ: from the classical diffusive regime found for $\sigma_s/\lambda > 1$ to the ballistic regime for $\sigma_s/\lambda < 0.01$, passing through the superdiffusive regime in between. Most interestingly, two subregimes could be distinguished within the superdiffusive regime according to their PDF $\Psi(\Lambda)$ distributions. Besides the conventional superdiffusive regime whose $\Psi(\Lambda)$ contains one single heavy-tailed peak, we identified an unconventional superdiffusive regime characterized by an oscillating $\Psi(\Lambda)$. This unconventional superdiffusive regime sheds light on the quasiballistic phonon transport and the competition between diffuse scattering and specular scattering in nanowires. The specular rates at the different boundaries revealed that phonons scatter less on the rough side boundaries due to a narrowing of the angle distribution around the long axis of the nanowire for high σ_s/λ ratios. We deduced that diffuse scattering at rough boundaries can tune the width of the angular distribution that determines the direction of propagation of the phonons, which can create directional phonon emitters. Finally, the behavior of the Lévy index as a function of the roughness-to-wavelength ratio suggests that an underlying law must exist. Further theoretical investigation to find this law would help understanding and controlling thermal transport in nanostructures.

ACKNOWLEDGMENT

This work was supported by the National Natural Science Foundation of China (Grant No. 89200419).

APPENDIX: PROBABILITY OF SUCCESSIVE SPECULAR SCATTERING

The probability to obtain n successive specular scattering events is given by P_S^n (with $n \in \mathbb{N}^*$) as each scattering event is independent. In Fig. 8 we set $A_i = 0°$ in Eq. (2) as the most probable angle according to Lambert's cosine law and we plot the probability P_S^n to obtain up to $n = 8$ successive specular scattering events.

Sawtooth oscillations appear in the PDF when P_S^n is high enough to allow several successive specular scattering events but not too close to 1 so as to diffusively scatter a significant fraction of the phonons. These conditions are met for $0.1 < \sigma/\lambda < 0.01$. After each scattering event, the fraction of diffusively scattered phonons generates a peak in the PDF at $\Lambda(n) = (n+1)W_n$, where $W_n = 100$ nm is the width of the nanowire. Each peak is followed by a heavy tail, indicating that the jump phase of the Lévy walk can persevere after multiple scattering events. Because $P_S^{n+1} < P_S^n$, the peak at $\Lambda(n+1)$ has a lower amplitude than the peak at $\Lambda(n)$. Hence, we obtain sawtooth oscillations with a 100-nm period and decreasing amplitude as the MFP increases, as observed in Fig. 5(f).

For $\sigma/\lambda > 0.1$, P_S^n is very low and almost all the phonons are diffusely scattered each time they reach a boundary, which yields a single peak at $\Lambda = 100$ nm. At the other end, for

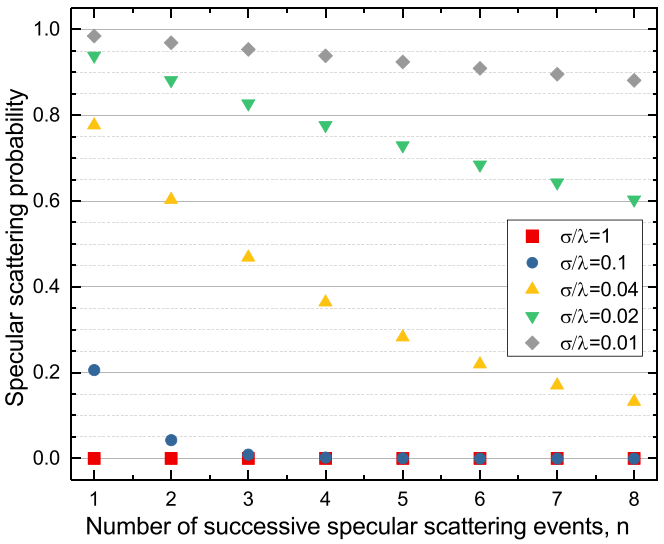

FIG. 8. Probability to obtain n successive specular scattering events.

$\sigma/\lambda < 0.01$, P_S^n is very high and decreases slowly. In this case, the fraction of diffusively scattered phonons is too small to create large enough peaks that exceed the statistical noise and the MFP is mainly limited by the length of the nanowire.

[1] R. B. Wilson and D. G. Cahill, Anisotropic failure of Fourier theory in time-domain thermoreflectance experiments, Nat. Commun. **5**, 5075 (2014).

[2] M. E. Siemens, Q. Li, R. Yang, K. A. Nelson, E. H. Anderson, M. M. Murnane, and H. C. Kapteyn, Quasi-ballistic thermal transport from nanoscale interfaces observed using ultrafast coherent soft X-ray beams, Nat. Mater. **9**, 26 (2010).

[3] V. Zaburdaev, S. Denisov, and J. Klafter, Lévy walks, Rev. Mod. Phys. **87**, 483 (2015).

[4] Y. Hu, L. Zeng, A. J. Minnich, M. S. Dresselhaus, and G. Chen, Spectral mapping of thermal conductivity through nanoscale ballistic transport, Nat. Nanotechnol. **10**, 701 (2015).

[5] J. Amrit, K. Nemchenko, and T. Vikhtinskaya, Effect of diffuse phonon boundary scattering on heat flow, J. Appl. Phys. **129**, 085105 (2021).

[6] N. Yang, G. Zhang, and B. Li, Violation of Fourier's law and anomalous heat diffusion in silicon nanowires, Nano Today **5**, 85 (2010).

[7] Z. Zhang, Y. Ouyang, Y. Cheng, J. Chen, N. Li, and G. Zhang, Size-dependent phononic thermal transport in low-dimensional nanomaterials, Phys. Rep. **860**, 1 (2020).

[8] A. Malhotra and M. Maldovan, Phononic pathways towards rational design of nanowire heat conduction, Nanotechnology **30**, 372002 (2019).

[9] R. Anufriev, Y. Wu, and M. Nomura, Ballistic heat conduction in semiconductor nanowires, J. Appl. Phys. **130**, 070903 (2021).

[10] W. Park, D. D. Shin, S. J. Kim, J. S. Katz, J. Park, C. H. Ahn, T. Kodama, M. Asheghi, T. W. Kenny, and K. E. Goodson, Phonon conduction in silicon nanobeams, Appl. Phys. Lett. **110**, 213102 (2017).

[11] X. Yang, A. C. To, and R. Tian, Anomalous heat conduction behavior in thin finite-size silicon nanowires, Nanotechnology **21**, 155704 (2010).

[12] G. Xie, Y. Guo, B. Li, L. Yang, K. Zhang, M. Tang, and G. Zhang, Phonon surface scattering controlled length dependence of thermal conductivity of silicon nanowires, Phys. Chem. Chem. Phys. **15**, 14647 (2013).

[13] T.-K. Hsiao, H.-K. Chang, S.-C. Liou, M.-W. Chu, S.-C. Lee, and C.-W. Chang, Observation of room-temperature ballistic thermal conduction persisting over 8.3μm in SiGe nanowires, Nat. Nanotechnol. **8**, 534 (2013).

[14] D. Vakulov, S. Gireesan, M. Y. Swinkels, R. Chavez, T. Vogelaar, P. Torres, A. Campo, M. De Luca, M. A. Verheijen, S. Koelling, L. Gagliano, J. E. M. Haverkort, F. X. Alvarez, P. A. Bobbert, I. Zardo, and E. P. A. M. Bakkers, Ballistic phonons in ultrathin nanowires, Nano Lett. **20**, 2703 (2020).

[15] J. Maire, R. Anufriev, and M. Nomura, Ballistic thermal transport in silicon nanowires, Sci. Rep. **7**, 41794 (2017).

[16] R. Anufriev, S. Gluchko, S. Volz, and M. Nomura, Quasi-ballistic heat conduction due to Lévy phonon flights in silicon nanowires, ACS Nano **12**, 11928 (2018).

[17] H. Kim, G. Park, S. Park, and W. Kim, Strategies for manipulating phonon transport in solids, ACS Nano **15**, 2182 (2021).

[18] X. Qian, J. Zhou, and G. Chen, Phonon-engineered extreme thermal conductivity materials, Nat. Mater. **20**, 1188 (2021).

[19] L. Yang, Y. Tao, Y. Zhu, M. Akter, K. Wang, Z. Pan, Y. Zhao, Q. Zhang, Y.-Q. Xu, R. Chen, T. T. Xu, Y. Chen, Z. Mao, and D. Li, Observation of superdiffusive phonon transport in aligned atomic chains, Nat. Nanotechnol. **16**, 764 (2021).

[20] W. Park, G. Romano, E. C. Ahn, T. Kodama, J. Park, M. T. Barako, J. Sohn, S. J. Kim, J. Cho, A. M. Marconnet, M. Asheghi, A. M. Kolpak, and K. E. Goodson, Phonon conduction in silicon nanobeam labyrinths, Sci. Rep. **7**, 6233 (2017).

[21] R. Anufriev, A. Ramiere, J. Maire, and M. Nomura, Heat guiding and focusing using ballistic phonon transport in phononic nanostructures, Nat. Commun. **8**, 15505 (2017).

[22] R. Yanagisawa, J. Maire, A. Ramiere, R. Anufriev, and M. Nomura, Impact of limiting dimension on thermal conductivity of one-dimensional silicon phononic crystals, Appl. Phys. Lett. **110**, 133108 (2017).

[23] K. Hippalgaonkar, B. Huang, R. Chen, K. Sawyer, P. Ercius, and A. Majumdar, Fabrication of microdevices with integrated nanowires for investigating low-dimensional phonon transport, Nano Lett. **10**, 4341 (2010).

[24] J. P. Feser, J. S. Sadhu, B. P. Azeredo, K. H. Hsu, J. Ma, J. Kim, M. Seong, N. X. Fang, X. Li, P. M. Ferreira, S. Sinha, and D. G. Cahill, Thermal conductivity of silicon nanowire arrays with controlled roughness, J. Appl. Phys. **112**, 114306 (2012).

[25] J. Lim, K. Hippalgaonkar, S. C. Andrews, A. Majumdar, and P. Yang, Quantifying surface roughness effects on phonon transport in silicon nanowires, Nano Lett. **12**, 2475 (2012).

[26] M. G. Ghossoub, K. V. Valavala, M. Seong, B. Azeredo, K. Hsu, J. S. Sadhu, P. K. Singh, and S. Sinha, Spectral phonon scattering from sub-10 nm surface roughness wavelengths in metal-assisted chemically etched Si nanowires, Nano Lett. **13**, 1564 (2013).

[27] J. M. Ziman, *Electrons and Phonons: The Theory of Transport Phenomena in Solids* (Oxford University Press, Oxford, 1960).

[28] A. A. Maznev, Boundary scattering of phonons: Specularity of a randomly rough surface in the small-perturbation limit, Phys. Rev. B **91**, 134306 (2015).

[29] S. B. Soffer, Statistical model for the size effect in electrical conduction, J. Appl. Phys. **38**, 1710 (1967).

[30] D.-S. Tang, Y.-C. Hua, and B.-Y. Cao, Thermal wave propagation through nanofilms in ballistic-diffusive regime by Monte Carlo simulations, Int. J. Therm. Sci. **109**, 81 (2016).

[31] A. Tavakoli, K. Lulla, T. Crozes, N. Mingo, E. Collin, and O. Bourgeois, Heat conduction measurements in ballistic 1D phonon waveguides indicate breakdown of the thermal conductance quantization, Nat. Commun. **9**, 4287 (2018).

[32] A. Ramiere, S. Volz, and J. Amrit, Geometrical tuning of thermal phonon spectrum in nanoribbons, J. Phys. D **49**, 115306 (2016).

[33] F. Yang and C. Dames, Mean free path spectra as a tool to understand thermal conductivity in bulk and nanostructures, Phys. Rev. B **87**, 035437 (2013).

[34] A. J. Minnich, Determining Phonon Mean Free Paths from Observations of Quasiballistic Thermal Transport, Phys. Rev. Lett. **109**, 205901 (2012).

[35] R. Anufriev and M. Nomura, Ray phononics: Thermal guides, emitters, filters, and shields powered by ballistic phonon transport, Mater. Today Phys. **15**, 100272 (2020).

[36] A. Malhotra and M. Maldovan, Impact of phonon surface scattering on thermal energy distribution of Si and SiGe nanowires, Sci. Rep. **6**, 25818 (2016).

[37] B. Vermeersch, J. Carrete, N. Mingo, and A. Shakouri, Superdiffusive heat conduction in semiconductor alloys. I. Theoretical foundations, Phys. Rev. B **91**, 085202 (2015).

[38] B. Vermeersch, A. M. S. Mohammed, G. Pernot, Y. R. Koh, and A. Shakouri, Superdiffusive heat conduction in semiconductor alloys. II. Truncated Lévy formalism for experimental analysis, Phys. Rev. B **91**, 085203 (2015).

[39] J. Klafter and G. Zumofen, Lévy statistics in a Hamiltonian system, Phys. Rev. E **49**, 4873 (1994).

[40] V. Zaburdaev, M. Schmiedeberg, and H. Stark, Random walks with random velocities, Phys. Rev. E **78**, 011119 (2008).